Inorganic Chemistry

Article

pubs.acs.org/IC

Structure–Function Relationships for Electrocatalytic Water Oxidation by Molecular $[Mn_{12}O_{12}]$ Clusters

Yong Yan, John S. Lee,† and Daniel A. Ruddy*

Chemistry and Nanoscience Center, National Renewable Energy Laboratory, Golden, Colorado 80401, United States

Supporting Information

ABSTRACT: A series of $Mn_{12}O_{12}(OAc)_{16-x}L_x(H_2O)_4$ molecular clusters (L = acetate, benzoate, benzenesulfonate, diphenylphosphonate, dichloroacetate) were electrocatalytically investigated as water oxidation electrocatalysts on a fluorine-doped tin oxide glass electrode. Four of the $[Mn_{12}O_{12}]$ compounds demonstrated water oxidation activity at pH 7.0 at varying overpotentials (640–820 mV at 0.2 mA/cm^2) and with high Faradaic efficiency (85–93%). For the most active complex, more than 200 turnovers were observed after 5 min. Two structure–function relationships for these complexes were developed. First, these complexes must undergo at least one-electron oxidation to become active catalysts, and complexes that cannot be oxidized in this potential window were inactive. Second, a greater degree of distortion at Mn1 and Mn3 centers correlated with higher catalytic activity. From this distortion analysis, either or both of these two Mn centers are proposed to be the catalytically active site.

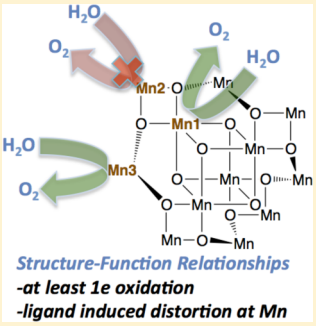

INTRODUCTION

Metal oxide-based materials are desirable for applications in photoelectrochemical (PEC) water splitting due to their general stability, and as such, have received considerable attention as water oxidation catalysts (WOCs).[1−4] The water oxidation reaction is considered to be the rate-limiting step in the overall water-splitting process and presents a formidable challenge of coordinating four proton-coupled electron transfers. Despite these challenges, promising recent advances have been achieved with a variety of oxide-based species, including bulk oxides, nanoparticles, and/or molecular oxo-bridged clusters of Ru, Co, and Mn.[5−10] These results represent significant achievements in the field, but there remains a continuing need to develop structure–function relationships to guide the design of new WOCs that are highly active, robust, and earth-abundant. The latter of these requirements makes Mn-based materials particularly interesting.

Mn cluster complexes based on the $[Mn_{12}O_{12}]$ core have received extensive research attention due to their behavior as single-molecule magnets.[11] However, these complexes have received little attention as oxidation catalysts, despite numerous attractive properties outlined by Christou et al.[12] Namely, these clusters hold promise based on the high oxidation state $Mn^{3+/4+}$ ions, the ability to undergo multiple reversible one-electron redox processes, the tunability of the ligand sphere, and the structural similarity to soluble pieces of catalytically active Mn oxide and the $CaMn_4O_x$ oxygen-evolving complex in PSII. The successful development of WOCs based on small Mn–oxo complexes, such as dimers and the cubane $Mn_4O_4L_6$, have demonstrated the efficacy of these properties at the molecular level and have provided insight into the catalytic mechanism at Mn centers.[13,14]

To gain the fundamental knowledge needed for the design of next-generation, earth-abundant WOCs, the investigation of large clusters, which can be viewed as truncated pieces of metal oxide, may provide a bridge between molecular catalysis and bulk oxide catalysis, for which there exists no detailed description of the catalytic surface sites.[8] For example, the Mn–O bond distances and angles in the $[Mn_{12}O_{12}]$ complexes are structurally well-defined by single-crystal X-ray diffraction, and if structure–function relationships can be developed at specific Mn sites in these clusters, they can be related to the catalytic performance of Mn oxides. However, because of the lack of catalysis research focusing on large clusters, there is a corresponding paucity of clear relationships between various structural motifs (e.g., ligands, Mn–O bond distances, angles, distortion) and their effect on catalytic performance.

To explore the WOC activity of large $[Mn_{12}O_{12}]$ clusters, we chose a series of complexes based on the parent acetate (OAc) compound, $Mn_{12}O_{12}(OAc)_{16}(H_2O)_4$ (**1**), and previously reported ligand-exchanged analogues having the general formula $Mn_{12}O_{12}(OAc)_{16-x}L_x(H_2O)_4$, where L is the exchanged ligand (Scheme 1): benzoate (**2**, x = 16), benzenesulfonate (**3**, x = 8), diphenylphosphonate (**4**, x = 8), and dichloroacetate (**5**, x = 16).[15−19] For comparison, the

Scheme 1. Ligand Exchange Syntheses of $[Mn_{12}O_{12}]$ Complexes 2–5[15−19]

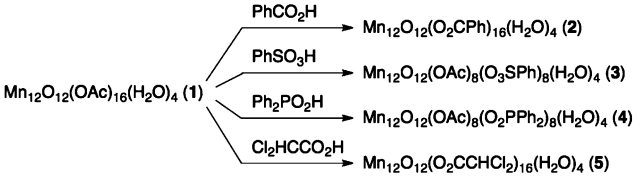

Received: February 20, 2015
Published: April 17, 2015

DOI: 10.1021/acs.inorgchem.5b00398
Inorg. Chem. 2015, 54, 4550−4555

cubane $Mn_4O_4(O_2PPh_2)_6$ (**6**), a known Mn-based WOC cluster, was also synthesized.[20−22] Here we report the electrocatalytic water oxidation performance at pH 7.0 of complexes **1**−**6** after dispersion on fluorine-doped tin oxide (FTO) electrodes. Four of the $[Mn_{12}O_{12}]$ complexes demonstrated water oxidation activity with high Faradaic efficiencies. Two structure−function relationships were identified for these complexes, and mechanistic implications at the specific Mn sites are presented.

EXPERIMENTAL SECTION

General. Acetonitrile (electrochemical grade 99.999%, trace metal basis) was purchased from Sigma-Aldrich and was used as received. Tetrabutylammonium hexafluorophosphate was purified by recrystallization from absolute ethanol three times. Complexes **1**−**6** and $[Mn_4O_3(OH)](O_2PPh_2)_6$ (**6H**) were prepared according to their respective literature procedures,[15−20] and their purity was confirmed as reported. The FTO transparent conducting glass substrate (TEC15) was purchased from Sigma-Aldrich. Prior to use, the FTO was cleaned by soaking in 5 wt % NaOH in ethanol for 16 h and then rinsing it sequentially with deionized (DI) water, ethanol, and water.

Characterization. Cyclic voltammetry (CV) measurements were recorded using a CH instruments potentiostat and a three-electrode cell consisting of a glassy carbon working electrode, Pt mesh counter electrode, and Ag/AgCl reference electrode.[23−25] The supporting electrolyte was 0.1 M tetrabutylammonium hexafluorophosphate; complexes **1**−**5** were recorded in acetonitrile, and **6** was recorded in dichloromethane (Supporting Information, Figure S1a−f). Electrocatalysis was performed in an aqueous solution of 0.5 M potassium phosphate at pH 7.0 (KPi) with a scan rate of 100 mV/s, with a Pt mesh counter electrode and a Ag/AgCl reference electrode. Polarization-corrected curves were obtained by averaging the measured currents of the forward and reverse CV data, according to the recently reported procedure.[26] Visible absorbance spectroscopy of **1**−**6** and **6H** in solution, and the working electrodes after deposition of **1**−**6** on FTO were measured using a Cary 6000i UV−vis spectrophotometer, using the bare FTO electrode as a background.

Preparation of $[Mn_{12}O_{12}]$/Fluorine-Doped Tin Oxide Working Electrodes. Immediately before catalyst loading, the FTO substrates were sonicated in ethanol for 10 min and then in DI water for 20 min. A freshly prepared acetonitrile solution of catalyst was dropcast using a micropipet onto a masked 1 cm^2 of the FTO glass.[23] The amount of solution corresponded to a total loading of each catalyst of 5.0 nmol.

Oxygen Evolution Experiments. A four-neck round-bottom flask was charged with 25 mL of KPi electrolyte and a magnetic stir bar. Three necks were equipped with the three electrodes, respectively, and the fourth neck was equipped with an Ocean-Optics HIOXY oxygen sensor. The sensor was operated by a NEOFOX-GT oxygen phase fluorimeter with RS232 communication. New septa were used for each experiment, and the electrode/septum interfaces were further sealed against leaks by applying silicone grease. The Pt mesh counter electrode in the same electrolyte was separated from the working compartment by a glass frit, which allows current flow but prevents mass exchange between the working and counter electrode compartments. For the working electrode, a copper wire was inserted through the septum, and an alligator clip was used to connect this copper wire to the FTO electrode. The active area of the working electrode was then fully submersed in the electrolyte. Note that during the course of the experiment, the alligator clip must avoid contact with the electrolyte. Two needles were inserted through the fourth septum. One needle was used to purge the system with nitrogen, and the other was used to balance the pressue in the sealed system.

Before the measurement, nitrogen was sparged through the system for at least 30 min, and the oxygen concentration in the solution was monitored using the oxygen sensor. After 30 min, a stable oxygen concentration below 0.1 ppm was achieved. This oxygen level was stable for at least 15 min after removing the gas in/out needles. Electrocatalytic activity was evaluated at a potential of 1.5 V versus Ag/AgCl, and the oxygen concentration was recorded using the NEOFOX-GT system. The headspace oxygen was also measured. Before electrolysis, the headspace oxygen concentration was below the detection limit of our sensor. Dissovled oxygen diffuses to the gaseous headspace as described by Henry's law; however, due to the low dissolved oxygen levels generated by the $[Mn_{12}O_{12}]$ catalysts during the short time of electrolysis (maxium 1.1 ppm by catalyst **4** after 5 min), the headspace oxygen concentration after electrolysis was still below the detection limit. Therefore, oxygen dissolution due to Henry's law can be neglected, and the dissolved oxygen values determined by the sensor represent the total oxygen generated in this system.

Catalyst Leaching/Deposition Experiments. The experimental setup was identical to that described for oxygen evolution experiments. These exeperiments were conducted by replacing the active **4**/FTO electrode after 60 s of electrocatalysis, and replacing with a bare FTO electrode. Electrocatalytic current versus time was recorded. Similarly, experiments were performed where the **4**/FTO working electrode and bare FTO working electrode were switched back and forth.

^{18}O-Labeled Water Oxidation. Electrocatalysis using ^{18}O isotopically labeled water was conducted similarly to oxygen evolution experiments above; however, the reaction volume was significantly reduced to ensure accurate headspace analysis. A 10 mL single neck flask was charged with 1 mL of KPi electroylte having 28 mol % $H_2{}^{18}O$, and the three electrodes were inserted through a septum. The solution was sparged with nitrogen for 30 min. Electrocatalysis was begun as described above. The headspace gas was transferred by a pressure-lock precision analytical syringe (VICI Precision Sampling, Inc.) and O_2 isotopes were analyzed by GC-MS (Agilent Technologies: GC, 7890A; MS, 5975C inertXL MSD with triple-Axis Detectors). In general, the labeled $^{34}O_2$ product was observed with at least 10 times higher intensity than natural abundance, and $^{36}O_2$ product was observed with more than 1000 times increased intensity than natural abundance. The theoretical ratio for $^{34}O_2/^{36}O_2$ for oxygen being exclusively generated from water of 28 mol % $H_2{}^{18}O$ was calcuated to be 5.15. The natural abundance of this ratio is 1003, consistent with experiments using unlabeled water.

RESULTS AND DISCUSSION

To prepare a typical electrode for use in catalytic testing, 20−30 μL of a 0.5−1 mg/mL acetonitrile solution of the complex was dropcast onto an FTO glass electrode at 60 °C. Catalyst loading was controlled at 5 nmol, and the electrode surface area was masked to ensure a 1 cm^2 electroactive surface. This approach is similar to the reported analysis of a Ru dimer for WOC activity on an indium tin oxide electrode.[23] Visible absorbance spectroscopy was used to investigate the structures of the deposited complexes versus their characteristic solution spectra (Supporting Information, Figure S2). The absorbance spectra for the $[Mn_{12}O_{12}]$ complexes **1**−**5** were found to be essentially identical to their respective solution spectra, indicating no significant structural changes (e.g., ligand loss leading to core distortion, oxidation/reduction) on FTO. For the $[Mn_4O_4]$ cubane **6** on FTO, an additional low-energy peak in the absorbance spectrum was observed versus **6** in solution. The spectrum for **6**/FTO matches the related, previously reported complex $[Mn_4O_3(OH)](O_2PPh_2)_6$ (**6H**), the product of a proton-coupled electron transfer (PCET) to **6**.[20] This structure is assigned to the surface-bound species for **6**/FTO, presumably formed through PCET from the FTO semiconductor (Figure S2). For our purposes of comparing **6** as a reference WOC, this structural change for **6**/FTO is considered minor since it retains the cubane core and all six phosphonate ligands. Furthermore, **6H** has been thoroughly investigated with respect to its redox chemistry to/from **6**, and the complex

DOI: 10.1021/acs.inorgchem.5b00398
Inorg. Chem. 2015, 54, 4550−4555

can access the proposed intermediate structures of water oxidation as reported for **6**.[20]

The electrocatalytic water oxidation activity of **1**–**6** on FTO was first evaluated by CV in 0.5 M KPi (pH 7.0). It is important to point out that the bare FTO substrate generates an oxidative current in the examined potential window. Control experiments conducted with ligands deposited on FTO (i.e., no $[Mn_{12}O_{12}]$) were identical to bare FTO. However, complexes **1**–**4** and **6** each exhibit significantly greater current density than the FTO background (Figure 1). An oxidative current of 1.94 mA/cm^2 at

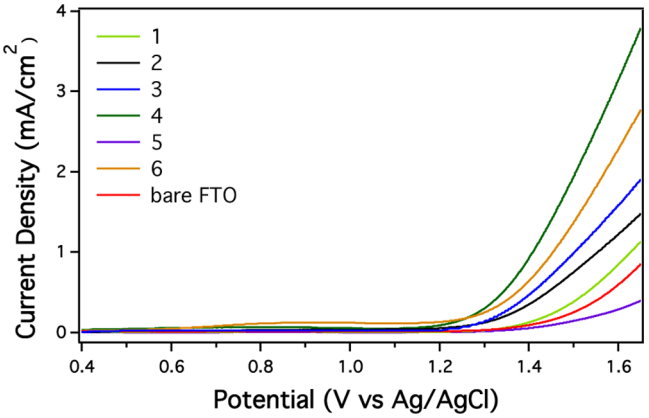

Figure 1. Polarization-corrected CV curves of **1**–**6** on an FTO glass electrode in 0.5 M KPi (pH 7.0).

1.5 V was observed for the most active complex **4**, which is more active than the known WOC cubane **6** (1.38 mA/cm^2 at 1.5 V) under these conditions. The current density values at this potential for all complexes are listed in Table 1 and follow

Table 1. Electrochemical Properties of 1–6 and Their Catalytic Activity for Water Oxidation on Fluorine-Doped Tin Oxide Electrodes

	E_{ox}[a] (V)	E_{red} (V)	η[c] (V)	i[d] (mA/cm^2)	TON[e]	FY[f] (%)
1	1.47; 1.26	0.63	0.82	0.39	36	85
2	1.25	0.55	0.77	0.78	44	85
3	1.51; 1.25	0.66	0.70	1.01	91	87
4	1.34; 1.07	0.55	0.64	1.94	210	93
5	>1.7[b]	1.30	0.94	0.13		
6	1.10		0.67	1.38	160	93
FTO			0.86	0.24		

[a]Redox potentials recorded in 0.1 M $[Bu_4N][PF_6]$ in MeCN (**6** in CH_2Cl_2) with a glassy carbon working electrode, Ag/AgCl reference, and Pt mesh counter electrode (Supporting Information, Figure S1). [b]Oxidation of **5** was outside the solvent potential window. [c]The thermodynamic potential for water oxidation is 0.62 V vs Ag/AgCl at pH 7; overpotential was determined at a polarization-corrected current density of 0.2 mA/cm^2. [d]Current density was determined at 1.5 V vs Ag/AgCl. [e]Turnover number (TON) is the total mol O_2 per mol catalyst after 5 min. [f]Faradaic yield (FY) was determined after 5 min.

the trend of **4** > **6** > **3** > **2** > **1**. The overpotential values are also given in Table 1, and although generally high overpotentials were observed, the values for the most active complexes, namely, **4** and **6**, are comparable to other Mn-based systems under similar conditions.[26−28]

To investigate the current efficiency of the observed oxidative current toward water oxidation, we employed an in situ O_2 sensor (Ocean Optics, HIOXY) to monitor electrocatalytic oxygen generation. Figure 2 displays the oxygen evolution plots versus time during electrolysis at 1.5 V (vs Ag/AgCl). The

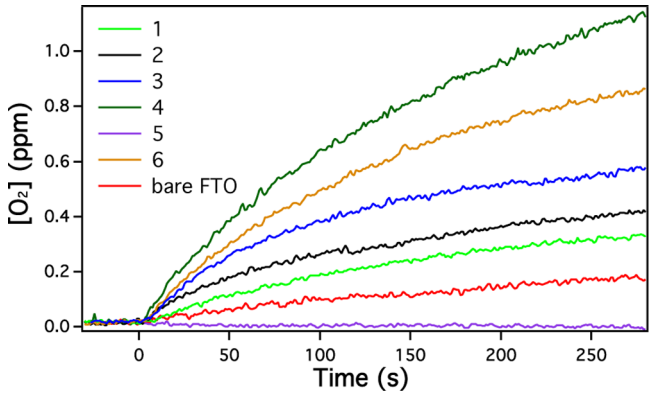

Figure 2. Real-time oxygen evolution plots during electrolysis at 1.50 V vs Ag/AgCl.

amount of evolved O_2 follows the order **4** > **6** > **3** > **2** > **1**, which is the same activity trend as suggested by the *I*–*V* data. The slopes of the plots, indicating the rate of oxygen generation, decreased after the first 60 s of electrolysis, and this suggests either decomposition, a structural distortion/change to the $[Mn_{12}O_{12}]$ core, or loss of the catalyst. The visible absorbance spectrum of an electrode before and after electrolysis was compared to explore changes to the catalyst. After 60 s of electrolysis, a clear change in the absorbance was observed versus the original spectrum, and this was more pronounced after 5 min of electrolysis (Supporting Information, Figure S3). The spectra suggest structural changes or decomposition of the original $[Mn_{12}O_{12}]$ complex, but some loss of the complex cannot be ruled out. The chemical information on the new structure(s) are currently unknown; however, on the basis of the decrease in O_2 evolution, they appear to be catalytically inactive under these conditions. To explore leaching of the $[Mn_{12}O_{12}]$ species and redeposition as an active catalyst, control experiments were conducted where the working electrode **4**/FTO was switched with bare FTO after 60 s (Supporting Information, Figure S4a) and cycled back and forth with bare FTO (Supporting Information, Figure S4b). The catalytic current disappears when the **4**/FTO electrode is removed, and the bare FTO does not exhibit any activity that would be associated with electrodeposition of free, active species. Further, reinsertion of the original **4**/FTO electrode after rinsing results in reappearance of the catalytic current, suggesting the active species remains intact on the original electrode.

The overall current efficiencies (FY) and turnover numbers (TON) after 5 min are also listed in Table 1. Complexes **1**–**4** and **6** demonstrate a high efficiency for oxygen generation (85–93%), with **4** and **6** exhibiting the highest Faradaic yields of 93%. For the most active catalyst, **4**, 210 turnovers were observed. When compared to the amount of **4** that was loaded onto the electrode, this TON corresponds to 34 times the amount of O_2 contained in the $[Mn_{12}O_{12}]$ core and 10 times the amount of total oxygen (Supporting Information, Table S1). Oxidation of ^{18}O-labeled water was also performed, and the measured $^{34}O_2/^{36}O_2$ ratio of 5.19 ± 0.02 was in good agreement with the theoretical value of 5.15 based on our experimental conditions (28 mol % ^{18}O, Supporting Information, Table S2). These data indicate that the observed

DOI: 10.1021/acs.inorgchem.5b00398
Inorg. Chem. 2015, 54, 4550−4555

O_2 truly originates from water, rather than catalyst decomposition. Multiple experiments with **4** demonstrated good reproducibility, within ±16% for TON and ±1.4% for FY. However, there was greater irreproducibility when employing **6**, where multiple experiments were within ±40% in TON and ±2.0% in FY.

Electrodes prepared with **5** demonstrated extremely low current density and no oxygen production (Figures 1 and 2). This complex exhibited values that were lower than the bare FTO substrate, suggesting that the inert complex covered the FTO surface and prevented the background reaction. Complex **5** employs the dichloroacetate ligand, which provides a strong electron-withdrawing effect and results in a first oxidation potential that is outside of the experimental window for acetonitrile (Table 1). This oxidation potential (>1.7 V) is markedly more positive than the values for complexes **1**–**4** and **6** (1.07–1.26 V). Detailed investigations have been reported for **6**, which has demonstrated activity as a photoactive WOC on a Nafion electrode under illumination,[22] and it has been shown that **6** must undergo one-electron oxidation before WOC activity is observed. For our series of complexes, each one can be oxidized at least once within the explored potential window except **5**, and this provides an important data point for the first structure–function relationship for these $[Mn_{12}O_{12}]$-based catalysts: similar to **6**, the $[Mn_{12}O_{12}]$ catalysts must undergo a one-electron oxidation prior to observing catalytic activity.

For heterogeneous Mn–oxide WOCs, the Mn–O distances, the Mn valencies, and the distortion around the Mn center have been proposed to be critical parameters that could be used to construct structure–function relationships.[8,26] For example, the greater catalytic efficiency demonstrated by bixbyite–Mn_2O_3 was attributed to the longer Mn–O bonds associated with Mn^{3+}, which were described as weaker and more flexible Mn–O bonds than other Mn oxides.[8] However, it has also been recently reported that such distances played a marginal role for a $Li_{2-x}MnP_2O_7$ system (x = 0, 0.3, 0.5, 1), and in contrast, a greater WOC activity was observed for materials with shorter Mn–O bond lengths.[26] For these $Li_{2-x}MnP_2O_7$ catalysts, a distortion analysis was presented for Mn sites having different valencies. The greater WOC activity demonstrated by $LiMnP_2O_7$ (x = 1) was attributed to the Jahn–Teller effect associated with the presence of Mn^{3+} centers. This distortion is not prevalent for other Mn valence states, such as Mn^{4+}, and the materials with lower distortion correspondingly demonstrated lower WOC activity. Each $[Mn_{12}O_{12}]$ complex explored here formally contains 8 Mn^{3+} and 4 Mn^{4+} centers, and crystallographic analysis shows that there are negligible differences between the average Mn–O bond lengths for **1**–**4**, likely due to their similar ligation (Supporting Information, Table S3).[15−19] However, similar to the evaluation of the $Li_{2-x}MnP_2O_7$ system, crystal structure analyses of **1**–**4** undoubtedly demonstrate different degrees of Mn distortion (Δ), as calculated using Baur's equation (eq 1),[29]

$$\Delta = \sum_{i=1}^{N} \frac{|d_i - d_m|}{N \times d_m} \quad (1)$$

where d_i and d_m are the individual and mean values of Mn–O bond lengths, and N is the total bond number. Table 2 lists the distortion indices for each type of distinct Mn site in the crystal structure, as depicted in Figure 3. The distortion indices for the Mn2 sites in all $[Mn_{12}O_{12}]$ complexes are similar, and no trend was observed. However, the distortion indices for Mn1 (cubane core) and Mn3 (aqua-ligated) sites correlate remarkably well with the relative catalytic performance (**4** > **6** > **3** > **2** > **1**), where greater activity and Faradaic yield are associated with complexes having higher distortion at these two sites. For example, **4** exhibited the highest catalytic activity and was determined to have the largest Mn1 distortion (0.025), which was greater than that of **2** and **3** (0.015, 0.017) and nearly three times greater than that of **1** (0.009). Complex **6** only contains Mn1 sites, and these have a distortion index value that is less than that of **4**, but similar to those of **2** and **3**, which again parallels the relative catalytic performance demonstrated by **6**. It is worth noting that the coordination environment for **6** is vastly different from the $[Mn_{12}O_{12}]$ clusters, but the distortion analysis accurately describes the relative activity of this small cluster under these conditions. Similar results were obtained after analysis of the Mn3 sites. The highly symmetric **1**, which displayed the lowest activity, exhibited a single, low distortion index value for all Mn3 sites (0.045). The Mn3 indices of **2** and **3** (two Mn3 sites) were determined to be moderate values between those for **1** and **4**. For the most active complex **4**, the highest distortion index value was observed (0.079). This value is ca. 1.5 times greater than the average index for the most active and most distorted $LiMnP_2O_7$ catalyst (0.054). However, the distortion index value greatly differed for each of the four unique Mn3 sites in **4**, in agreement with the reported low symmetry in this complex due to the bulky and π-stacking phosphonate ligands.[19] For this series of $[Mn_{12}O_{12}]$ clusters, the distortion analysis provides a critical structure–function relationship between the local bonding at the Mn sites and the corresponding WOC activity.

It is interesting to consider possible mechanistic pathways for these newly identified $[Mn_{12}O_{12}]$ catalysts. Complexes **1**–**4** contain a cubic core similar to that of **6**, consisting of four Mn1 sites, which has been proposed to form a Mn_4O_2-"butterfly" intermediate when releasing O_2 during its catalytic cycle. When comparing the structures of **1**–**4** with bixbyite–Mn_2O_3 and $LiMnP_2O_7$, aqua-ligated Mn3 sites resemble the surface Mn

Table 2. Mn Distortion Index Values for 1–4 as Determined from Their Crystal Structures

	Mn1	Mn2	Mn3a	Mn3b	Mn3c	Mn 3d
1	0.009	0.068	0.045	0.045	0.045	0.045
2	0.015	0.064	0.063	0.065		
3	0.017	0.055	0.064	0.065		
4	0.025	0.065	0.079	0.066	0.053	0.051
6	0.016					

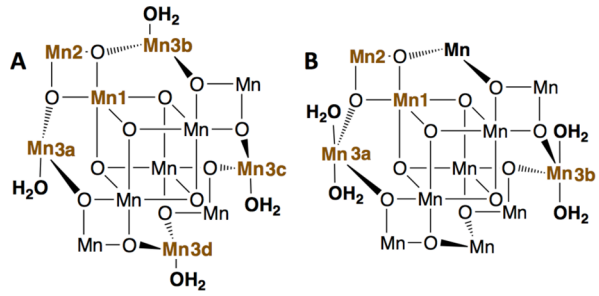

Figure 3. Concise structural representations of (A) **1** and **4** and (B) **2** and **3**, based on the reported crystal structures. The distinct Mn sites are notated, along with the different binding environments of H_2O at Mn3 sites. Mn are all six-coordinate in the complexes, but OAc and L ligands were omitted for clarity.

DOI: 10.1021/acs.inorgchem.5b00398
Inorg. Chem. 2015, 54, 4550–4555

active sites of those heterogeneous catalysts, which are proposed to be the water-binding site during catalysis.[8,26] Considering the structural similarities of **1**−**4** with **6** and with Mn oxides, and the strong correlation between the WOC activity and Mn1/Mn3 distortion indices, we propose that the active site of the $[Mn_{12}O_{12}]$ catalysts is at the Mn1 and/or Mn3 site. At the Mn1 site, the $[Mn_{12}O_{12}]$ catalysts may follow a similar pathway to that proposed for **6**, progressing through a "butterfly" intermediate during O_2 formation. Water oxidation may also proceed through consecutive deprotonations to form the high-valent Mn(V)−oxo at the Mn3 site, followed by O_2 elimination similar to previously proposed mechanisms for an aqua-ligated Mn_2O_2 dimer.[10,13]

CONCLUSIONS

Four previously reported $[Mn_{12}O_{12}]$ complexes were newly identified as water oxidation electrocatalysts, with the highest activity exhibited by the mixed-ligand acetate−phosphonate complex **4**. The first oxidation potential was found to be an important property for these complexes, since they must undergo at least one-electron oxidization to become active catalysts. The Baur distortion index was calculated from the single-crystal X-ray structures for the series of complexes, and there was a clear relationship between complexes having greater Mn distortions and enhanced catalytic performance. This distortion analysis was previously applied to a heterogeneous Mn oxide system, and we have demonstrated that the structure−function relationship derived from this analysis may be more broadly applicable to molecular catalysts. This analysis may provide an approach to identify new WOCs from the large library of known $[Mn_xO_x]$ cluster complexes and to design new complexes as synthetic targets. Finally, this approach supports the utilization of cluster complexes as models for oxide-based catalysts to investigate key structural features and to extend this approach toward the elucidation of catalytic mechanisms and intermediates to aid the design of next-generation oxide catalysts.

ASSOCIATED CONTENT

Supporting Information

Electrochemical characterization of **1**−**6**; visible absorbance spectra for **1**−**6**, **6H**, and after deposition on FTO; visible absorbance spectra before and after electrocatalysis for **4**/FTO; electrocatalysis data for cycling **4**/FTO and bare FTO working electrodes; values for the determination of TON and FY; results from ^{18}O-labeled water experiments; and average Mn−O bond distances for **1**−**6**. This material is available free of charge via the Internet at http://pubs.acs.org.

AUTHOR INFORMATION

Corresponding Author

*E-mail: dan.ruddy@nrel.gov.

Present Address

[†]Dept. of Chemistry, Univ. of California-Berkeley, Berkeley, CA.

Author Contributions

The manuscript was written through contributions of all authors. All authors have given approval to the final version of the manuscript.

Notes

The authors declare no competing financial interest.

ACKNOWLEDGMENTS

The authors thank J. Gu and N. R. Neale for helpful discussions. This research was supported by NREL's Laboratory Directed Research & Development (LDRD) program under U.S. Dept. of Energy Contract No. DE-AC36-08-GO28308. This research was supported in part (J.S.L.) by the U.S. Dept. of Energy, Office of Science, Office of Workforce Development for Teachers and Scientists (WDTS) under the Science Undergraduate Laboratory Internship (SULI) program.

REFERENCES

(1) Barber, J. *Chem. Soc. Rev.* **2009**, *38*, 185.
(2) Turner, J. A. *Science* **2004**, *305*, 972.
(3) Walter, M. G.; Warren, E. L.; McKone, J. R.; Boettcher, S. W.; Mi, Q. X.; Santori, E. A.; Lewis, N. S. *Chem. Rev.* **2010**, *110*, 6446.
(4) Gu, J.; Yan, Y.; Krizan, J. W.; Gibson, Q. D.; Detweiler, Z. M.; Cava, R. J.; Bocarsly, A. B. *J. Am. Chem. Soc.* **2014**, *136*, 830.
(5) Concepcion, J. J.; Tsai, M. K.; Muckerman, J. T.; Meyer, T. J. *J. Am. Chem. Soc.* **2010**, *132*, 1545.
(6) Esswein, A. J.; McMurdo, M. J.; Ross, P. N.; Bell, A. T.; Tilley, T. D. *J. Phys. Chem. C* **2009**, *113*, 15068.
(7) Kanan, M. W.; Nocera, D. G. *Science* **2008**, *321*, 1072.
(8) Robinson, D. M.; Go, Y. B.; Mui, M.; Gardner, G.; Zhang, Z. J.; Mastrogiovanni, D.; Garfunkel, E.; Li, J.; Greenblatt, M.; Dismukes, G. C. *J. Am. Chem. Soc.* **2013**, *135*, 3494.
(9) Yin, Q. S.; Tan, J. M.; Besson, C.; Geletii, Y. V.; Musaev, D. G.; Kuznetsov, A. E.; Luo, Z.; Hardcastle, K. I.; Hill, C. L. *Science* **2010**, *328*, 342.
(10) Rumberger, E. M.; Ahn, H. S.; Bell, A. T.; Tilley, T. D. *Dalton Trans.* **2013**, *42*, 12238.
(11) Bagai, R.; Christou, G. *Chem. Soc. Rev.* **2009**, *38*, 1011.
(12) Maayan, G.; Christou, G. *Inorg. Chem.* **2011**, *50*, 7015.
(13) Limburg, J.; Vrettos, J. S.; Liable-Sands, L. M.; Rheingold, A. L.; Crabtree, R. H.; Brudvig, G. W. *Science* **1999**, *283*, 1524.
(14) Dismukes, G. C.; Brimblecombe, R.; Felton, G. A. N.; Pryadun, R. S.; Sheats, J. E.; Spiccia, L.; Swiegers, G. F. *Acc. Chem. Res.* **2009**, *42*, 1935.
(15) Lis, T. *Acta Crystallogr., Sect. B* **1980**, *36*, 2042.
(16) Sessoli, R.; Tsai, H. L.; Schake, A. R.; Wang, S. Y.; Vincent, J. B.; Folting, K.; Gatteschi, D.; Christou, G.; Hendrickson, D. N. *J. Am. Chem. Soc.* **1993**, *115*, 1804.
(17) Boskovic, C.; Pink, M.; Huffman, J. C.; Hendrickson, D. N.; Christou, G. *J. Am. Chem. Soc.* **2001**, *123*, 9914.
(18) Soler, M.; Chandra, S. K.; Ruiz, D.; Huffman, J. C.; Hendrickson, D. N.; Christou, G. *Polyhedron* **2001**, *20*, 1279.
(19) Chakov, N. E.; Wernsdorfer, W.; Abboud, K. A.; Hendrickson, D. N.; Christou, G. *Dalton Trans.* **2003**, 2243.
(20) Carrell, T. G.; Bourles, E.; Lin, M.; Dismukes, G. C. *Inorg. Chem.* **2003**, *42*, 2849.
(21) Ruettinger, W. F.; Campana, C.; Dismukes, G. C. *J. Am. Chem. Soc.* **1997**, *119*, 6670.
(22) Brimblecombe, R.; Swiegers, G. F.; Dismukes, G. C.; Spiccia, L. *Angew. Chem., Int. Ed.* **2008**, *47*, 7335.
(23) Wada, T.; Tsuge, K.; Tanaka, K. *Angew. Chem., Int. Ed.* **2000**, *39*, 1479.
(24) Yan, Y.; Chandrasekaran, P.; Mague, J. T.; DeBeer, S.; Sproules, S.; Donahue, J. P. *Inorg. Chem.* **2012**, *51*, 346.
(25) Yan, Y.; Zeitler, E. L.; Gu, J.; Hu, Y.; Bocarsly, A. B. *J. Am. Chem. Soc.* **2014**, *135*, 14020.
(26) Park, J.; Kim, H.; Jin, K.; Lee, B. J.; Park, Y. S.; Kim, H.; Park, I.; Yang, K. D.; Jeong, H. Y.; Kim, J.; Hong, K. T.; Jang, H. W.; Kang, K.; Nam, K. T. *J. Am. Chem. Soc.* **2014**, *136*, 4201.
(27) Jin, K.; Park, J.; Lee, J.; Yang, K. D.; Pradhan, G. K.; Sim, U.; Jeong, D.; Jang, H. L.; Park, S.; Kim, D.; Sung, N. E.; Kim, S. H.; Han, S.; Nam, K. T. *J. Am. Chem. Soc.* **2014**, *136*, 7435.
(28) Takashima, T.; Hashimoto, K.; Nakamura, R. *J. Am. Chem. Soc.* **2012**, *134*, 1519.

DOI: 10.1021/acs.inorgchem.5b00398
Inorg. Chem. 2015, 54, 4550−4555

(29) Baur, W. H. *Acta Crystallogr., Sect. B* **1974**, *30B*, 1195.

DOI: 10.1021/acs.inorgchem.5b00398
Inorg. Chem. 2015, 54, 4550−4555